Letter

Theory of dispersive optical phonons in resonant inelastic x-ray scattering experiments

Krzysztof Bieniasz [1,2,*] Steve Johnston [3,4,†] and Mona Berciu [1,2,‡]

[1]*Quantum Matter Institute, University of British Columbia, Vancouver, British Columbia, Canada V6T 1Z4*
[2]*Department of Physics and Astronomy, University of British Columbia, Vancouver, British Columbia, Canada V6T 1Z1*
[3]*Department of Physics and Astronomy, University of Tennessee, Knoxville, Tennessee 37996, USA*
[4]*Institute for Advanced Materials and Manufacturing, University of Tennessee, Knoxville, Tennessee 37996, USA*

(Received 13 January 2022; accepted 18 April 2022; published 9 May 2022)

The community currently lacks a complete understanding of how resonant inelastic x-ray scattering (RIXS) experiments probe the electron-phonon interaction in solids. For example, most theoretical models of this process have focused on dispersionless Einstein phonons. Using a recently developed momentum average variational approximation for computing RIXS spectra of band insulators, we examine the influence of both electron and phonon dispersion in the intermediate state of the scattering process. We find that the inclusion of either, and their mutual interplay, introduces significant momentum variations in the RIXS intensity, even for momentum-independent electron-phonon coupling. The phonon dispersion also induces nontrivial changes in the excitation line shapes, which can have a quantitative impact on the data analysis. These results highlight the considerable challenges of interpreting RIXS data in actual materials.

DOI: 10.1103/PhysRevB.105.L180302

Introduction. Resonant inelastic x-ray scattering (RIXS) [1,2] is being used increasingly to study electron-phonon (*e*-ph) coupling in solids. This application is being driven by the steady improvements of both the instrument resolution and our understanding of the RIXS cross section. For example, theoretical modeling has suggested that RIXS can access the *e*-ph coupling strength with momentum resolution and element specificity [3–5].

One of the most popular methods for quantitatively analyzing lattice excitations in RIXS spectra is the single-site framework developed by Ament *et al.* [3]. It approximates the infinite system with a single isolated site whose local electron density in the valence orbital couples to the lattice displacements. This simplified model's exact RIXS scattering amplitude can be computed within the Kramers-Heisenberg formalism using a Lang-Firsov transformation. Its key predictions are that the *e*-ph coupling produces a series of low-energy harmonic excitations in the energy-loss spectra, whose relative intensities can be mapped onto the strength of the *e*-ph interaction.

Whereas this single-site model has been widely employed for data analysis [6–10], its approximations are drastic, and it is unclear how relaxing them may affect the results of the analysis. For this reason, several groups have attempted to develop alternative approaches. Examples (in no particular order) include generalizations of the single-site framework to include multiple modes or changes in the harmonic potential in the intermediate state [11], exact diagonalization of small clusters [4,12], diagrammatic approaches [5,13], cumulant expansions of the Green's function [14], and dynamical mean-field theory [15].

Recently, we introduced an efficient variational method for computing RIXS spectra for band insulators [16]. Our method is built on the momentum average (MA) class of variational approximations [17,18] and allows us to treat situations where a core electron is excited into an empty band in the intermediate state of the RIXS process and is allowed to interact with the lattice. We showed that the single-site approximation becomes inaccurate for shallower core-hole potentials and found that the itinerancy of the valence electron leads to momentum dependence in the intensity of the RIXS phonon peaks even if both the *e*-ph coupling and the phonon's dispersion are momentum independent. Naturally, this raises the question of whether the momentum dependence of various features in the RIXS spectra can be used to infer momentum dependence of either the *e*-ph coupling and/or the phonon dispersion.

Here, we answer the latter part of this question. We extend the MA formalism to study band insulators where the excited electron couples to *dispersive* optical phonons. Our goal is to understand how a finite phonon bandwidth affects the RIXS spectra when the *e*-ph coupling is momentum independent (Holstein). We find that the phonon bandwidth produces specific $\boldsymbol{q}$ dependence of the multiphonon excitations so that even for a Holstein coupling, we obtain single- and multiphonon excitations whose peak location and intensity vary significantly around the first Brillouin zone. Moreover, the predicted multiphonon line shapes are complicated, deviating considerably from the Lorentzian or Gaussian shapes frequently adopted when fitting experimental data. These results expand our knowledge of how the details of the *e*-ph coupling are encoded in the RIXS cross section and further underscore the need to move beyond single-site models in data analysis.

*krzysztof.t.bieniasz@gmail.com
†sjohn145@utk.edu
‡berciu@phas.ubc.ca

The model. We examine the RIXS spectra for a band insulator whose valence electrons are coupled to a dispersive optical phonon branch in the intermediate state of the scattering process. The Hamiltonian is $\mathcal{H} = \mathcal{H}_e + \mathcal{H}_{\text{ph}} + \mathcal{H}_{e\text{-ph}} + \mathcal{H}_{\text{ch}}$. Here,

$$\begin{aligned}\mathcal{H}_e &= -t \sum_{\langle ij \rangle} [d_i^\dagger d_j + \text{H.c.}] \\ &= \sum_{\boldsymbol{k}} \epsilon_{\boldsymbol{k}} d_{\boldsymbol{k}}^\dagger d_{\boldsymbol{k}} \end{aligned} \tag{1}$$

where $d_i^\dagger$ (d_i) creates (annihilates) an electron at site i in the valence band, and $\epsilon_{\boldsymbol{k}}$ is the valence-band dispersion. The optical phonon is described by

$$\mathcal{H}_{\text{ph}} = \sum_{\boldsymbol{q}} \omega_{\boldsymbol{q}} b_{\boldsymbol{q}}^\dagger b_{\boldsymbol{q}}, \tag{2}$$

where $b_{\boldsymbol{q}}^\dagger$ ($b_{\boldsymbol{q}}$) creates (annihilates) a phonon with energy $\omega_{\boldsymbol{q}}$ (we set $\hbar = 1$). Throughout, we assume that the system is a two-dimensional square lattice with $a = 1$ so that $\epsilon_{\boldsymbol{k}} = -2t(\cos k_x + \cos k_y)$ whereas $\omega_{\boldsymbol{q}} = \omega_0 + 2\omega_1(\cos q_x + \cos q_y)$. Since we have in mind optical oxygen modes in transition-metal oxides, we further assume that the phonon bandwidth is small $\omega_1 \ll \omega_0$. The Holstein e-ph coupling is

$$\mathcal{H}_{e\text{-ph}} = \frac{g}{\sqrt{N}} \sum_i e^{-i\boldsymbol{k}\cdot\boldsymbol{R}_i} d_i^\dagger d_i \, (b_{\boldsymbol{k}}^\dagger + b_{-\boldsymbol{k}}), \tag{3}$$

where g is the strength of the coupling and N is the number of lattice sites. Finally,

$$\mathcal{H}_{\text{ch}} = \epsilon_{\text{ch}} \sum_i p_i^\dagger p_i - U_Q \sum_i d_i^\dagger d_i \, (1 - p_i^\dagger p_i) \tag{4}$$

describes the core-hole and its interaction with the valence electron. Specifically, $p_i^\dagger$ (p_i) creates (annihilates) an electron in the relevant core level at site i, ϵ_{ch} is the on-site energy of the core level, and $-U_Q$ is the local *attractive* interaction between the valence electron and the core hole. We use a mixed notation for the Holstein coupling [Eq. (3)] where the electron (phonon) operators are represented in real (momentum) space for later convenience. Finally, Eq. (4) captures the core-hole's influence on the system in the intermediate state via a local core-hole potential. We note that although the bare U_Q potential is purely local, the effective potential can extend over the entire lattice (albeit decaying very fast away from the core hole) [16,19,20] once dressed by the e-ph interaction.

The method. Our starting point is the standard Kramers-Heisenberg equation for the RIXS intensity [1,2], which we reformulate by expanding the δ function as the imaginary part of a final-state Green's function [21],

$$I(\boldsymbol{q}, \omega) = -\frac{1}{\pi} \text{Im} \sum_f \frac{|F_{fg}(\boldsymbol{q}, z)|^2}{\omega + i\eta - E_f + E_g}. \tag{5}$$

Here, η is a broadening parameter, and F_{fg} is the scattering amplitude,

$$F_{fg}(\boldsymbol{q}, z) = \sum_{n,i} e^{i\boldsymbol{q}\cdot\boldsymbol{R}_i} \frac{\langle f | D_i^\dagger | n \rangle \langle n | D_i | g \rangle}{E_g - E_n + z}, \tag{6}$$

where $|g\rangle$, $|n\rangle$, and $|f\rangle$ are the initial, intermediate, and final states of the RIXS process with energies E_g, E_n, and E_f, respectively, $z = \omega_{\text{in}} + i\Gamma$, ω_{in} and ω_{out} are the energies of the incident and scattered x-ray, and $\omega = \omega_{\text{out}} - \omega_{\text{in}}$ and $\boldsymbol{q}$ are the energy and momentum transferred to the sample, Γ is the inverse core-hole lifetime, and D_i is the dipole operator. (Here, we have omitted the geometric prefactors associated with the dipole matrix elements to focus on the effects of the electron and phonon dispersions.) The specific elemental edge does not matter at our level of modeling [16].

We briefly explain here our variational approach, delegating all details to the Supplemental Material [22]. The first step is to evaluate the spectral amplitude F_{fg}. Following Ref. [16], we cast it as a generalized propagator,

$$\mathcal{F}_{fg}(\boldsymbol{q}, z) = \frac{1}{\sqrt{N}} \sum_i e^{i\boldsymbol{q}\cdot\boldsymbol{R}_i} \langle f | \, p_i^\dagger d_i \, \mathcal{G}(z) d_i^\dagger p_i \, | g \rangle \, , \tag{7}$$

where $\mathcal{G}(z) = [z - \mathcal{H} + E_g]^{-1}$. We generate an equation of motion (EOM) for $\mathcal{F}_{fg}(z)$ by applying the Dyson identity $\mathcal{G}(z) = \mathcal{G}_0(z) + \mathcal{G}(z)\mathcal{V}\mathcal{G}_0(z)$, where $\mathcal{V} = \mathcal{H}_{e\text{-ph}}$ and $\mathcal{H}_0 = \mathcal{H} - \mathcal{H}_{e\text{-ph}}$ has the associated resolvent $\mathcal{G}_0(\omega)$. The EOM for $\mathcal{F}_{fg}(z)$ depends on new propagators, whose EOMs depend on other new propagators, etc., generating an infinite hierarchy of coupled EOMs. To simplify it, and then solve it, we define a variational Hilbert space characterized by the size and spread of the phonon cloud [18] and only keep in the hierarchy the EOMs for propagators consistent with this variational choice. In particular, it has been well documented that for a Holstein coupling that is not deep into the adiabatic regime, a one-site cloud approximation is very accurate. Deep in the adiabatic regime, Holstein polaron clouds spread over several consecutive sites, and the variational space needs to be expanded accordingly [23,24]. We implement this one-site cloud variational solution here. We emphasize that this polaron cloud can appear anywhere in the system, it is not restricted to the core-hole site. Additional technical details can be found in the Supplemental Material [22] as well as Refs. [16–18].

Results and discussion. Figure 1 presents RIXS spectra for an itinerant electron, Holstein coupled to a dispersive optical phonon branch. Here we take $\omega_0 = 1$ as our unit of energy and set $\omega_1 = 0.02\omega_0$, $t = 5\omega_0$, $g = 2\omega_0$, $U_Q = 20\omega_0$, and $\Gamma = 2\omega_0$ unless otherwise stated. The effective e-ph coupling $\lambda = g^2/4t\omega_0 = 0.2$ is, thus, rather weak. For a typical transition-metal oxide, we expect $\omega_0 \sim 100$ meV. Our value for Γ is, therefore, halfway between values appropriate of the transition-metal L edge and oxygen K edge [4,8,11]. Our choice for U_Q is smaller than the $U_Q \sim$ 4–6 eV typically adopted in the literature [4,12,25–27]. This choice partially accounts for the interaction between the core hole and the lattice and accentuates the delocalization effects in the intermediate state. As discussed previously [16], the core-hole-lattice coupling, which is neglected in Eq. (3), can frustrate polaron formation in the valence band. At the lowest order, this effect *reduces* the effective core-hole potential, which we account for by reducing U_Q.

For reference, Fig. 1(a) shows the RIXS spectrum for a dispersionless optical phonon ($\omega_1 = 0$). It shows the expected multiphonon excitations located at multiples $n\omega_0$ of the phonon energy. The excitations have Lorentzian line shapes

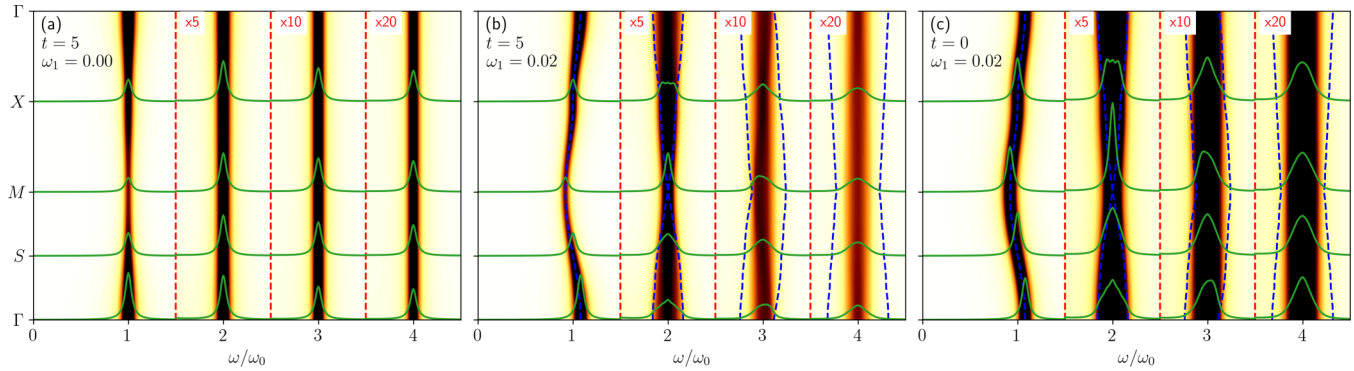

FIG. 1. RIXS spectra calculated for various model parameters. The results plotted for momentum transfers $\boldsymbol{q}$ along the high-symmetry cuts of the first Brillouin zone of the square lattice. The high-symmetry points are denoted as $\Gamma = (0, 0)$, $M = (1, 1)$, $X = (1, 0)$, and $S = (1/2, 1/2)$ in units of π/a. All results were obtained with a variational constraint $p = 2$ (see the Supplemental Material [22] for more details). (a) Mobile electron coupled to an Einstein phonon ($t = 5$ and $\omega_1 = 0$); (b) mobile electron coupled to a dispersive optical phonon ($t = 5$ and $\omega_1 = 0.02$); (c) localized electron coupled to a dispersive optical phonon branch ($t = 0$ and $\omega_1 = 0.02$). All parameters are in units of $\omega_0 = 1$. We have multiplied the intensity of the multiphonon peaks by the factor indicated in the corner of the respective region. The dashed blue lines indicate the edges of the corresponding multiphonon energy convolution (see the text for more details). The green lines are plots of the RIXS spectrum at the high-symmetry points.

with a broadening set by $\eta = 0.04\omega_0$ to mimic the instrument's resolution. The amplitude of the peaks decreases as the excitation number n increases. (For more clarity, we scaled each overtone by the numerical factor indicated in red at the top of the plot.) The momentum dependence of the intensity of the first phonon peak is due to the electron mobility in the intermediate state [16]. The intensity of the multiphonon peaks is $\boldsymbol{q}$ dependent, but it is harder to discern on this scale.

Figure 1(b) shows the RIXS spectrum when we introduce a phonon dispersion with a narrow bandwidth $\omega_1 = 0.02\omega_0$. The single-phonon peak continues to be a Lorentzian with broadening η, but its position now follows the phonon dispersion ω_q, indicated by the dashed blue line, as required by the conservation of momentum and energy [3,5]. Its intensity again exhibits a significant momentum dependence due to the mobility of the electron in the intermediate state. This is further confirmed by the RIXS spectrum shown in Fig. 1(c) for a localized electron ($t = 0$ and $\omega_1 = 0.02\omega_0$). Indeed, here the single-phonon peak tracks the phonon frequency $\omega_{\boldsymbol{q}}$ but has the same intensity at all values of $\boldsymbol{q}$.

Much more important is the observation that now the higher-order peaks in Fig. 1(b) also show a strong momentum dependence both in their line shape and intensity. To understand it, consider first the two-phonon peak. Here, the total transferred momentum is distributed between the two phonons left behind after the RIXS process, $\boldsymbol{q} = \boldsymbol{q}' + \boldsymbol{q}''$. The transferred energy must then equal the two phonons' energy

$$\omega_{\boldsymbol{q}-\boldsymbol{q}'} + \omega_{\boldsymbol{q}'} = 2\omega_0 + 4\omega_1 \sum_{\delta=x,y} \cos\frac{q_\delta}{2} \cos\left(q'_\delta - \frac{q_\delta}{2}\right)$$

There is no broadening at the M-point [$= (\pi, \pi)$] (apart from the extrinsic broadening η); however, for any other $\boldsymbol{q}$, the two-phonon peak has an intrinsic broadening $8\omega_1(\cos\frac{q_x}{2} + \cos\frac{q_y}{2})$, marked by the blue dashed lines due to the convolution over all $\boldsymbol{q}'$ values.

We can explain the broadening of the higher multiphonon peaks in a similar manner; it results from the convolution over the n-phonon energies with total momentum $\boldsymbol{q} = \sum_{i=1}^{n} \boldsymbol{q}_i$. The expected outermost energies allowed by this constraint are shown by the dashed blue lines and indeed mark the regions with finite RIXS intensity. The higher-order peaks, thus, exhibit an ever-growing broadening. For example, the four-phonon feature is approximately twice as wide as the two-phonon one. Figure 1(c) shows the same broadening for the localized electron, confirming that this feature is due solely to the phonon dispersion. These findings naturally explain why many experiments have resolved increasing linewidths for the multiphonon excitations [4,12].

Another interesting observation is that the shape of the two- and three-phonon peaks is highly nontrivial and does not follow a Lorentzian or Gaussian lineshape as is often assumed. Furthermore, the three-phonon peak is skewed, producing asymmetric peaks around the Γ and M points. The bond-stretching "breathing" phonon modes in transition-metal oxides often have bandwidths reminiscent of our model [28] whereas Cu L-edge RIXS experiments can access momentum transfers approaching the X point. Therefore, copper oxide materials could serve as a platform for experimentally confirming these effects, provided the coupling is strong enough to generate multiphonon excitations and depending on the instrumental resolution and the actual self-energy broadening of the valence electron. Nonetheless, it seems to be worth investigating. For example, it might be worth examining how incoherent, extremely correlated Fermi liquid [29,30] or non-Fermi liquid [31] behavior would manifest here.

The higher phonon excitations eventually revert to a Gaussian line shape as evident in the four-phonon line, owing to the central limit theorem (the crossover from unusual to Gaussian lineshapes is controlled by the strength of the e-ph coupling). In contrast to the case of a dispersionless phonon [panel (a)], we also see a stronger momentum dependence of the weight of the higher-phonon peaks. Comparison with panel (c) reveals that its details depend on the phonon and valence-band's bandwidth. We expect that this intensity and

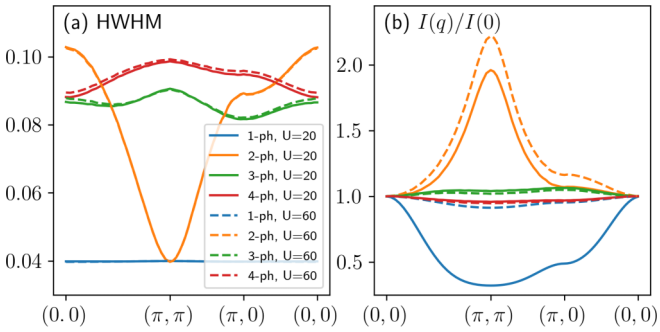

FIG. 2. An analysis of the phonon excitations for $\omega_0 = 1$, $t = 5\omega_0$, $\omega_1 = 0.02\omega_0$, $\Gamma = 2\omega_0$, and $g = 2\omega_0$. (a) The width of the phonon excitations, defined as the empirically determined half-width half maximum (HWHM) of the peak as a function of momentum. (b) The momentum dependence of the maximum phonon excitation intensity, normalized to their peak intensity at (0,0). In all panels, results are shown for the first four-phonon excitations and for $U_Q = 20\omega_0$ (solid lines) and $U_Q = 60\omega_0$ (dashed lines).

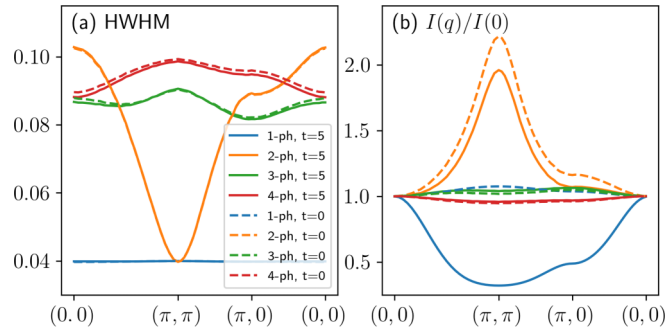

FIG. 3. An analysis of the phonon excitations for localized ($t = 0$, dashed lines) and delocalized ($t = 5\omega_0$, solid lines) electrons, similar to Fig. 2. Other parameters are $\omega_0 = 1$, $\omega_1 = 0.02\omega_0$, $U_Q = 20\omega_0$, and $g = 2\omega_0$.

the specific lineshapes will be further affected by a momentum dependence of the e-ph coupling, but the study of this issue is deferred to future work.

Figure 1 clearly illustrates that both electron mobility and phonon dispersion, and their interplay, produce phonon excitations with nontrivial momentum dependence in the RIXS spectra. We further quantify these results in Fig. 2 for different values of U_Q. Figures 2(a) and 2(b) plot the linewidth of the phonon peaks and their intensity as a function of momentum as obtained from numerical fitting of a Lorentzian lineshape. Here, the peak intensity is determined from the peak maximum. One could use the integrated area instead, which would show similar trends but with quantitative differences (not shown). The HWHM is used as proxy for the peak width. For $U_Q = 20\omega_0$, the intensity of the first and second phonon excitations varies significantly. For example, the first phonon excitation drops in intensity by more than half when tracking from $(0,0)$ to (π,π), whereas the intensity of the second phonon excitation grows by a factor of 2. As discussed, the width of the first phonon peak is fixed to our input resolution ($\eta = 0.04\omega_0$), whereas the width of the second phonon peak varies by more than 100% following the trends noted previously. In comparison, the momentum dependence of the third and fourth phonon excitations is weaker but remains significant.

We also examine a larger core-hole potential $U_Q = 60\omega_0$. This value effectively localizes the excited valence electron at the core-hole site in the intermediate state and reduces the momentum dependence of the phonon peaks (similar to the $t = 0$ results). The only exception is the two-phonon peak, which still varies rapidly as a function of $\boldsymbol{q}$. This result suggests that the largest contribution to the momentum dependence of two-phonon excitation arises from the phonon dispersion rather than the electron mobility. To confirm this, Fig. 3 compares the results of the same analysis, this time for systems with $t = 0$, $t = 5\omega_0$, and $U_Q = 20\omega_0$. The strong similarity between the results for the localized electron ($t = 0$) and those obtained for a mobile electron with $U_Q = 60\omega_0$, indicate that this larger potential is indeed strong enough to localize the electron in the intermediate state.

Summary and conclusions. Our results demonstrate that electron mobility and phonon dispersion produce momentum-dependent phonon excitations in the RIXS spectra. Crucially, this dependence emerges even for models with *momentum independent* e-ph interactions and would significantly impact estimates for the strength of the coupling if one does not account for it. We also found that the phonon dispersion produces a nontrivial broadening of the multiphonon excitations. This effect may account for the increasing widths of the phonon excitations often observed in experiments [4,12].

Our results have important implications for analyzing RIXS data on systems with dispersive phonon modes. For example, the single-site model predicts that the strength of the e-ph coupling can be directly extracted from the intensity ratios of successive phonon excitations with $g_{\boldsymbol{q}}/\Gamma = I_{n+1}(\boldsymbol{q})/I_n(\boldsymbol{q})$ [3]. In our model, g is independent of $\boldsymbol{q}$ yet the resulting $I_n(\boldsymbol{q})$ functions are not, showing that this simple mapping does not hold for dispersive systems. Importantly, this conclusion holds in the limit of strong electron localization (i.e., strong, attractive core-hole potentials) if the relevant phonon branch has a sizable bandwidth.

Our results are for a band insulator where the core electron is excited into an empty band in the intermediate state of the scattering process. We suggest that such systems, along with other dilute materials, could be used to develop a controlled theory of e-ph coupling in RIXS experiments. In the future, it is highly desirable to explore these effects in cases where the band is partially filled and/or where correlation effects cannot be neglected.

Acknowledgments. K.B. and M.B. acknowledge support from the UBC Stewart Blusson Quantum Matter Institute (SBQMI) and the Natural Sciences and Engineering Research Council of Canada (NSERC). S.J. was supported by the National Science Foundation under Grant No. DMR-1842056.

[1] A. Kotani and S. Shin, Rev. Mod. Phys. **73**, 203 (2001).

[2] L. J. P. Ament, M. van Veenendaal, T. P. Devereaux, J. P. Hill, and J. van den Brink, Rev. Mod. Phys. **83**, 705 (2011).

[3] L. J. P. Ament, M. van Veenendaal, and J. van den Brink, Europhys. Lett. **95**, 27008 (2011).

[4] W. S. Lee, S. Johnston, B. Moritz, J. Lee, M. Yi, K. J. Zhou, T. Schmitt, L. Patthey, V. Strocov, K. Kudo, Y. Koike, J. van den Brink, T. P. Devereaux, and Z. X. Shen, Phys. Rev. Lett. **110**, 265502 (2013).

[5] T. P. Devereaux, A. M. Shvaika, K. Wu, K. Wohlfeld, C. J. Jia, Y. Wang, B. Moritz, L. Chaix, W.-S. Lee, Z.-X. Shen, G. Ghiringhelli, and L. Braicovich, Phys. Rev. X **6**, 041019 (2016).

[6] D. Meyers, K. Nakatsukasa, S. Mu, L. Hao, J. Yang, Y. Cao, G. Fabbris, H. Miao, J. Pelliciari, D. McNally, M. Dantz, E. Paris, E. Karapetrova, Y. Choi, D. Haskel, P. Shafer, E. Arenholz, T. Schmitt, T. Berlijn, S. Johnston, J. Liu, and M. P. M. Dean, Phys. Rev. Lett. **121**, 236802 (2018).

[7] M. Rossi, R. Arpaia, R. Fumagalli, M. Moretti Sala, D. Betto, K. Kummer, G. M. De Luca, J. van den Brink, M. Salluzzo, N. B. Brookes, L. Braicovich, and G. Ghiringhelli, Phys. Rev. Lett. **123**, 027001 (2019).

[8] L. Braicovich, M. Rossi, R. Fumagalli, Y. Peng, Y. Wang, R. Arpaia, D. Betto, G. M. De Luca, D. Di Castro, K. Kummer, M. Moretti Sala, M. Pagetti, G. Balestrino, N. B. Brookes, M. Salluzzo, S. Johnston, J. van den Brink, and G. Ghiringhelli, Phys. Rev. Research **2**, 023231 (2020).

[9] Y. Y. Peng, A. A. Husain, M. Mitrano, S. X.-L. Sun, T. A. Johnson, A. V. Zakrzewski, G. J. MacDougall, A. Barbour, I. Jarrige, V. Bisogni, and P. Abbamonte, Phys. Rev. Lett. **125**, 097002 (2020).

[10] Y. Peng, L. Martinelli, Q. Li, M. Rossi, M. Mitrano, R. Arpaia, M. M. Sala, Q. Gao, X. Guo, G. M. De Luca, A. Walters, A. Nag, A. Barbour, G. Gu, J. Pelliciari, N. B. Brookes, P. Abbamonte, M. Salluzzo, X. Zhou, K.-J. Zhou, V. Bisogni, L. Braicovich, S. Johnston, and G. Ghiringhelli, Phys. Rev. B **105**, 115105 (2022).

[11] A. Geondzhian and K. Gilmore, Phys. Rev. B **101**, 214307 (2020).

[12] S. Johnston, C. Monney, V. Bisogni, K.-J. Zhou, R. Kraus, G. Behr, V. N. Strocov, J. Málek, S.-L. Drechsler, J. Geck, T. Schmitt, and J. van den Brink, Nat. Commun. **7**, 10563 (2016).

[13] H. Y. Huang, A. Singh, C. Y. Mou, S. Johnston, A. F. Kemper, J. van den Brink, P. J. Chen, T. K. Lee, J. Okamoto, Y. Y. Chu, J. H. Li, S. Komiya, A. C. Komarek, A. Fujimori, C. T. Chen, and D. J. Huang, Phys. Rev. X **11**, 041038 (2021).

[14] C. D. Dashwood, A. Geondzhian, J. G. Vale, A. C. Pakpour-Tabrizi, C. A. Howard, Q. Faure, L. S. I. Veiga, D. Meyers, S. G. Chiuzbăian, A. Nicolaou, N. Jaouen, R. B. Jackman, A. Nag, M. García-Fernández, K.-J. Zhou, A. C. Walters, K. Gilmore, D. F. McMorrow, and M. P. M. Dean, Phys. Rev. X **11**, 041052 (2021).

[15] P. Werner and M. Eckstein, Phys. Rev. B **104**, 085155 (2021).

[16] K. Bieniasz, S. Johnston, and M. Berciu, SciPost Phys. **11**, 62 (2021).

[17] M. Berciu, Phys. Rev. Lett. **97**, 036402 (2006).

[18] M. Berciu and G. L. Goodvin, Phys. Rev. B **76**, 165109 (2007).

[19] M. Berciu, A. S. Mishchenko, and N. Nagaosa, Europhys. Lett. **89**, 37007 (2010).

[20] H. Ebrahimnejad and M. Berciu, Phys. Rev. B **85**, 165117 (2012).

[21] A. Nocera, U. Kumar, N. Kaushal, G. Alvarez, E. Dagotto, and S. Johnston, Sci. Rep. **8**, 11080 (2018).

[22] See Supplemental Material at http://link.aps.org/supplemental/10.1103/PhysRevB.105.L180302 for the details of the derivation of the variational method.

[23] D. J. J. Marchand, P. C. E. Stamp, and M. Berciu, Phys. Rev. B **95**, 035117 (2017).

[24] M. R. Carbone, D. R. Reichman, and J. Sous, Phys. Rev. B **104**, 035106 (2021).

[25] K. Okada and A. Kotani, Phys. Rev. B **63**, 045103 (2001).

[26] S. Kourtis, J. van den Brink, and M. Daghofer, Phys. Rev. B **85**, 064423 (2012).

[27] T. Tohyama, K. Tsutsui, M. Mori, S. Sota, and S. Yunoki, Phys. Rev. B **92**, 014515 (2015).

[28] L. Pintschovius, Phys. Status Solidi B **242**, 30 (2005).

[29] B. S. Shastry, Phys. Rev. Lett. **107**, 056403 (2011).

[30] P. Mai and B. S. Shastry, Phys. Rev. B **98**, 205106 (2018).

[31] T. J. Reber, N. C. Plumb, Z. Sun, Y. Cao, Q. Wang, K. McElroy, H. Iwasawa, M. Arita, J. S. Wen, Z. J. Xu, G. Gu, Y. Yoshida, H. Eisaki, Y. Aiura, and D. S. Dessau, Nat. Phys. **8**, 606 (2012).